JM PAPERS

Wall-attached structure characteristics of flow and dust concentration fields in high-Reynolds-number particle-laden flows

Xibo He[1], Hongyou Liu[1],† and Xiaojing Zheng[2]

[1]Center for Particle-laden Turbulence, Lanzhou University, Lanzhou 730000, PR China
[2]Research Center for Applied Mechanics, Xidian University, Xi'an 710071, PR China

The wall-attached structure characteristics of flow and dust concentration fields are investigated in this study based on high-Reynolds-number ($Re_\tau \sim O(10^6)$) synchronous multiphase observations from the Qingtu Lake observation array site (recorded by Liu *et al.*, *J. Fluid Mech.*, vol. 957, 2023, A14). The results show that not only the particle-free flow field but also the particle-laden flow and dust concentration field contain wall-attached structures. The linear coherence spectrum, as a data-driven filter, is adopted to separate the wall-attached portions from the premultiplied spectra. The decomposed spectra for wall-attached structures in streamwise velocity fluctuations under particle-free and particle-laden conditions show obvious outer-scaling and wall-scaling at large-scale and medium-scale ranges, respectively, but the spectra of dust concentration exhibit only wall-scaling rather than outer-scaling. The streamwise length of the most significant wall-attached dust clustering structures in the logarithmic region is approximately five times the boundary layer thickness, and does not change significantly with height. Furthermore, the streamwise turbulence intensity for wall-attached portions follows the universal Townsend–Perry constant, without particle mass loading effect. Correspondingly, the wall-attached portions of the dust concentration also exhibit universal logarithmic decay slope. The remaining non-attached portions for the turbulent velocity and dust concentration have significant dependence on the particle mass loading.

Key words: particle/fluid flow, atmospheric flows, turbulent boundary layers

1. Introduction

Coherent structures span a wide range of spatial/temporal scales in the flow field, and are important for generating and sustaining turbulence (Marusic *et al.* 2010; Jiménez 2012).

† Email address for correspondence: liuhongyou@lzu.edu.cn

Besides, these coherent structures, with a wide range of scales, play a vital role in the transport of heat, mass, momentum and energy, and have always been an open challenge for the study of high-Reynolds-number wall-bounded turbulence (Robinson 1991; Smits, McKeon & Marusic 2011; Liu & Zheng 2021). In addition, abundant particle motions exist in industrial equipment flows and atmospheric surface layer (ASL) flows, with friction Reynolds numbers Re_τ – the ratio of the outer length scale δ to the viscous length scale δ_ν, $Re_\tau \equiv \delta/\delta_\nu = \delta U_\tau/\nu$, where the outer length scale refers to the boundary layer thickness, half-height and radius for the turbulent boundary layer (TBL), channel and pipe flows, respectively, U_τ is the friction velocity, and ν is the kinetic viscosity – up to $O(10^6)$, and have a significant modulation effect on turbulence (Balachandar & Eaton 2010; Liu & Zheng 2021; Brandt & Coletti 2022). Studying the kinetic characteristics of fluids and particles plays a significant role in contributing further insights into high-Reynolds-number two-phase wall-bounded turbulence.

As a classic physical model in wall-bounded turbulence, the attached eddy model (AEM) was proposed by Townsend (1976) and was originally referred to as the attached eddy hypothesis (AEH). Under the AEH framework, the second-order statistical moments lead to

$$\left.\begin{aligned}
\langle u^2 \rangle^+ &= -A_1 \ln(z/\delta) + B_1, \\
\langle v^2 \rangle^+ &= -A_2 \ln(z/\delta) + B_2, \\
\langle w^2 \rangle^+ &= B_3,
\end{aligned}\right\} \tag{1.1}$$

where the angled brackets indicate time averages, and the superscript '+' indicates normalization using the friction velocity U_τ. Here, A_1, A_2, B_1, B_2 and B_3 are constants; in particular, A_1 is called the Townsend–Perry constant (Marusic *et al.* 2013; Vallikivi, Hultmark & Smits 2015*b*; Hwang, Hutchins & Marusic 2022). Owing to improvements in experimental equipment, a substantial amount of experimental research supporting the AEH has emerged and assessed its existence in wall turbulence (Marusic *et al.* 2013; Zhou & Klewicki 2015; Örlü *et al.* 2017). Marusic *et al.* (2013) analysed the experimental data in a nominal Reynolds number range $2 \times 10^4 < Re_\tau < 6 \times 10^5$ in channel, TBL, pipe and ASL flows; they noted the Townsend–Perry constants $A_1 = 1.21$ for channel, 1.26 for TBL, 1.23 for pipe and 1.33 for ASL (verified by Wang & Zheng 2016) within the experimental uncertainty for the measurement set. Subsequently, the Townsend–Perry constant A_1 was found to be weakly dependent on Reynolds number (Laval *et al.* 2017; Samie *et al.* 2018; Yamamoto & Tsuji 2018). Monkewitz (2022) proposed that the Townsend–Perry asymptotes to $A_1 = 0$ when $Re_\tau \to \infty$. In contrast, the Townsend–Perry constant should be invariant according to the AEH. In addition, Perry & Abell (1977) and Perry, Henbest & Chong (1986) contemplated that the energy spectra of streamwise fluctuating velocity $k_x \Phi_{uu}$ encompass three types of distinct structure energy contributions, which were further refined by Marusic & Perry (1995). Among these three types of eddies, Type-$\mathcal{A}$ eddies are attached to the wall and self-similar; only they can be described by the AEM, and they dominate the spectrum at ultra-high Re_τ (Marusic & Monty 2019; Baars & Marusic 2020*a*). Type-$\mathcal{B}$ eddies are physically large-scale detached eddies (Högström, Hunt & Smedman 2002; Baars & Marusic 2020*a*,*b*; Hu, Yang & Zheng 2020). Type-$\mathcal{C}$ eddies are smaller Kolmogorov-scale detached eddies that might be the remnant of eddies once attached to the wall in their lifetimes (Marusic & Monty 2019). A schematic diagram of the u energy spectrum for these three types of eddies is shown in figure 1.

According to the definition of the friction Reynolds number Re_τ, the larger the friction Reynolds number is, the more sufficient the scale separation of turbulent structures can
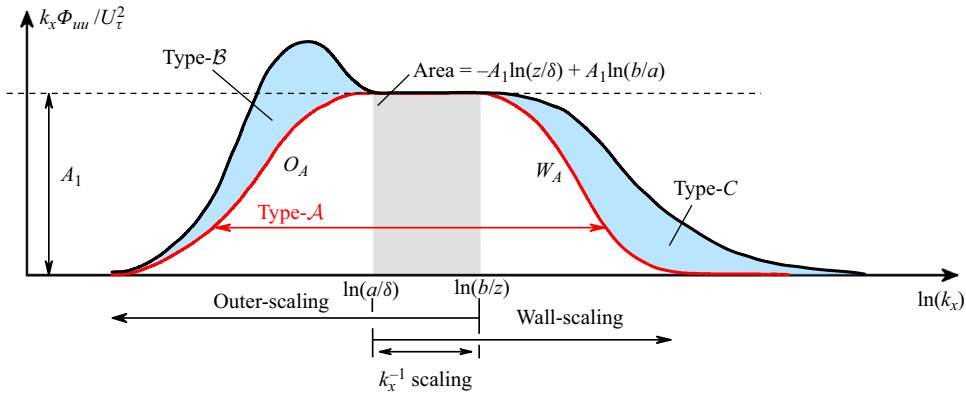
Figure 1. Schematic diagram of the *u* energy spectrum for the AEM of Perry *et al.* (1986). Here, another overlap region (i.e. inertial subrange) between wall-scaling and dissipation (Kolmogorov) scaling and the dissipation scaling region are ignored for simplicity.

be, the more obvious the logarithmic law signature is (Marusic *et al.* 2013), and the more abundant the hierarchical structures that can be captured theoretically. However, in real high-Reynolds-number flows, there are large-scale wall-detached coherent structures that significantly contribute to turbulence statistics in the logarithmic region (Guala, Hommema & Adrian 2006; Balakumar & Adrian 2007; Baars & Marusic 2020*a*,*b*). In other words, the statistical behaviours in the logarithmic layer can be contaminated by the contributions of wall-detached structures and the wall-attached non-self-similar structures that reach height δ – i.e. superstructures or very-large-scale motions (VLSMs) – which cannot be described by the AEH. This makes the statistical behaviours depart from the results predicted by the AEH (Baars & Marusic 2020*a*; Hu *et al.* 2020; Hwang, Lee & Sung 2020). Jiménez & Hoyas (2008) conducted channel simulations at $Re_\tau \leq 2000$, and pointed out that most of the drift and the poor logarithmic fit of velocity component *u* are due to the very long and wide eddies found in *u*. It is precisely because of the wall-detached eddy structures that the AEM cannot be verified directly according to the statistical characteristics of the flow field. Therefore, in the last two decades, different types of flow field decomposition methods have been proposed to extract wall-attached eddies in the flow field and then further verify the model, including the clustering method (del Álamo *et al.* 2006; Lozano-Durán, Flores & Jiménez 2012; Hwang & Sung 2018), bidimensional empirical mode decomposition (Cheng *et al.* 2019), proper orthogonal decomposition (POD; Hellström, Marusic & Smits 2016) and spectral decomposition (Hu *et al.* 2020). Hellström *et al.* (2016) performed stereo particle image velocimetry together with a POD analysis in fully developed turbulent pipe flow with $Re_\tau = 1330$ and 2460; they claimed that the resulting modes exhibit self-similar behaviour for a wide wall-normal length scale range. Hwang & Sung (2019) not only revealed that the detected structures are self-similar but also demonstrated their contribution to the mean velocity logarithmic law by leveraging the clustering method. Hu *et al.* (2020) proposed a decomposition scheme by limiting the range of the pre-multiplied energy spectra to extract a specific part of the velocity field; the resulting statistical behaviours can be well described by the AEH. To further investigate this significant self-similar characteristic, the linear coherence spectrum (LCS) is adopted as a statistical tool with the capability of efficiently inspecting the self-similarity of eddies (Baars, Hutchins & Marusic 2016, 2017; Marusic, Baars & Hutchins 2017; Baidya *et al.* 2019; Baars & Marusic 2020*a*,*b*), and the LCS

is formulated as

$$\gamma^2(z, z_R; \lambda_x) = \frac{|\langle \hat{u}(z; \lambda_x)\, \hat{u}^*(z_R; \lambda_x)\rangle|^2}{\langle |\hat{u}(z; \lambda_x)|^2 \rangle \langle |\hat{u}(z_R; \lambda_x)|^2 \rangle} = \frac{|\Phi_{uu}(z, z_R; \lambda_x)|^2}{\Phi_{uu}(z; \lambda_x)\, \Phi_{uu}(z_R; \lambda_x)}, \qquad (1.2)$$

where z_R and z are the spatial measurement heights for the reference and traversing points, respectively, $\hat{u}(z; \lambda_x)$ is the Fourier transform of $u(z; t)$, '$*$' denotes the complex conjugate, and $|\cdot|$ designates the modulus. Here, $\Phi_{uu}(z, z_R; \lambda_x)$ and $\Phi_{uu}(z; \lambda_x)$ are the cross-spectrum and power spectral spectrum, respectively, λ_x is the wavelength transformed from frequency f by Taylor's frozen hypothesis, where the convection velocity is taken as the local mean velocity $\bar{u}(z)$, i.e. $\lambda_x(z) = \bar{u}(z)/f(z)$, and $k_x(z) = 2\pi/\lambda_x(z)$ is the corresponding streamwise wavenumber. Obviously, the LCS is the ratio of the squared cross-spectrum magnitude relative to the product of the power spectral densities of u at z_R and z (Baars *et al.* 2016). The normalization of γ^2 occurs per scale, and for all scales, it is bounded within $0 \leq \gamma^2 \leq 1$, where $\gamma^2 = 0$ denotes the absence of coherence, and $\gamma^2 = 1$ indicates perfect coherence. Baars *et al.* (2017) investigated the self-similarity of coherent structures in TBL flows spanning a Reynolds number range $Re_\tau \sim O(10^3)$–$O(10^6)$ through the LCS, and the self-similarity of coherent structures was found to be described by a streamwise (λ_x) to wall-normal (z) aspect ratio 14. Then Krug *et al.* (2019) analysed the wind velocity and temperature under different thermal stratification conditions obtained from the surface layer turbulence and environmental science test (SLTEST) by means of the LCS, and observed that not only streamwise velocity fluctuations u, but also spanwise velocity fluctuations v and temperature fluctuations θ show obvious self-similar scaling, which is consistent with expectations based on the AEH framework. Baidya *et al.* (2019) conducted experiments on pipe ($10\,000 < Re_\tau < 39\,500$) and TBL ($Re_\tau = 14\,000$) flows with hot-wire and azimuthal/spanwise-spaced skin friction sensors, and analysed the coherence between the streamwise velocity and reference skin friction signals. They noted that wall-attached structures in the logarithmic layer exhibit obvious self-similarity, which decreases with increasing azimuthal/spanwise offset. Baars & Marusic (2020*a*,*b*) proposed a data-driven triple decomposition method on the basis of spectral coherence to extract the energy associated with wall-attached motions from TBL and ASL data spanning three decades in $Re_\tau \sim O(10^3)$–$O(10^6)$. Based on universal trends across all considered Reynolds numbers, some evidence has been given for a Townsend–Perry constant $A_1 = 0.98$, which would describe the wall-normal logarithmic decay of the turbulence intensity per Townsend's AEH. To obtain the wall-attached coherent structure characteristics in high-Reynolds-number flows, many intuitive and effective extraction methods have been proposed. However, due to the limitations of experimental facilities and computational capability, there has been no attempt to analyse the influence of particles on the wall-attached characteristics in more complex high-Reynolds-number particle-laden flows.

In the particle-laden turbulence research community, with increasing in-depth research, particles have been found to show the tendency to aggregate in the flow field. Particles in turbulence exhibit non-uniform spatial distribution, which is a phenomenon highly dependent on the Stokes number (St), defined as the ratio between the particle response time (τ_p) and a relevant fluid time scale (τ_f) (Berk & Coletti 2020; Brandt & Coletti 2022). Since the pioneering work of Maxey (1987), many early studies have supplied evidence that inertial particles are more likely to be centrifuged out of high-vorticity regions, causing them to preferentially concentrate in the high-strain regions between vortices (Squires & Eaton 1991; Elghobashi & Truesdell 1992). Later, this phenomenon of preferential concentration was widely observed for different types of

flows (McLaughlin 1989; Kaftori, Hetsroni & Banerjee 1995*a*,*b*; Niño & Garcia 1996; Picano, Sardina & Casciola 2009; Sardina *et al.* 2011, 2012). In addition to observing the aggregation characteristics of particles in the flow field directly, many studies have focused on the relationships between particle clustering/transport and turbulent structures (Kiger & Pan 2002; Marchioli & Soldati 2002; Bernardini, Pirozzoli & Orlandi 2013; Baker *et al.* 2017; Wang & Richter 2020; Jie *et al.* 2022). To investigate the effects of large-scale turbulence on particle dispersion, the particle distributions in Poiseuille flow and Couette flow with similar Reynolds numbers were compared in Bernardini *et al.* (2013). Owing to the large-scale structures in Couette flow, they observed large-scale particle streaks in Couette flow, with larger streamwise length and wider spanwise spacing than the near-wall small-scale streaks in Poiseuille flow. A recent experimental study of TBLs at $Re_\tau = 19\,000$ (Berk & Coletti 2020) showed that particles favour ejection events in a wide range of viscous Stokes numbers ($St^+ \equiv \tau_p U_\tau^2/\nu = 18\text{--}870$), i.e. they are often found in low-speed, upward-moving regions. Under higher-Reynolds-number conditions, dust concentration structures in scalar fields with streamwise scales exceeding 3δ, which are similar to the VLSMs in the flow field, are found in particle-laden ASLs ($Re_\tau \sim O(10^6)$) (He & Liu 2023). In addition, since the kinematics of particles is influenced by turbulent coherent structures, the multi-scale characteristics of coherent structures are also presented in particle clustering (Cui, Ruhman & Jacobi 2022; Jie *et al.* 2022). Overall, considerable information on coherent particle clusters has been discovered in recent years. However, the connections and differences between these clusters and turbulent motions, especially under higher-Reynolds-number conditions ($Re_\tau \sim O(10^6)$), remain open, where the scale separation is more significant and the motions are more abundant.

In summary, wall-attached structures in the flow field have been considered widely. Since there are other types of eddies in high-Reynolds-number flows, various types of eddy/flow extraction techniques have been proposed for extracting wall-attached eddies, and the extracted results are compared with the scaling law provided by the classic AEM. However, in typical high-Reynolds-number flows ($Re_\tau \sim O(10^6)$), studies on the wall-attached characteristics of the flow field and the corresponding particle effects are scarce. Moreover, the wall-attached characteristics of dust concentration under the influence of turbulent structures have yet to be reported. Therefore, the present work investigates the wall-attached characteristics of the flow field (in particle-free and particle-laden conditions) and dust concentration field based on high-Reynolds-number particle-free/laden data from long-term ASL observations.

The remaining parts of this work are organized as follows. Brief descriptions of the observation site, equipment and data pre-processing methods used are provided in § 2. The wall-attached characteristics of the flow field (in particle-free and particle-laden conditions, respectively), as well as those of the dust concentration field, are identified in § 3. Spectral scalings of fluctuating streamwise velocity and dust concentration, are presented in § 4. The classic Townsend–Perry constant is discussed in § 5. Finally, concluding remarks are offered in § 6.

2. Experiments and data processing

The Qingtu Lake observation array (QLOA), for studies on high-Reynolds-number canonical TBL layers as well as sand-laden two-phase flows, has been built in Minqin, China, and observational data have been accumulated in recent years. The array contains 1 main 32 m tower and 23 5 m towers set in the Cartesian coordinate system. Eleven sonic anemometers (CSAT3B, Campbell Scientific) with sampling frequency 50 Hz

are equipped logarithmically on the main tower from $z = 0.9$ to 30 m to measure the three components of wind velocities (u, v and w in the streamwise, spanwise and wall-normal directions, respectively) and the temperature. Moreover, based on the light scattering method (Shaughnessy & Morton 1977), eleven aerosol monitors (DUSTTRAK II-8530-EP, TSI Incorporated) with sampling frequency 1 Hz were installed on the main tower at the same height as the sonic anemometers to collect the concentration information of PM10 (particles with sizes smaller than $10 \, \mu m$). A panorama view of the QLOA, a schematic diagram of the installation of various probes, and additional details on the experimental set-up can be found in Liu, He & Zheng (2023).

Limited by the complex and uncontrollable nature of the ASL, not all the data are suitable for the study of wall turbulence. Therefore, rigorous data pre-processing is required to select suitable turbulence data. Following standard practice in the analysis of ASL data (Wyngaard 1992), the synchronously raw measured data are divided into multiple hourly time series to ensure statistical convergence (also confirmed by Ogive analysis) of the data and the corresponding spectra for subsequent processing (Hutchins *et al.* 2012). The data processing methods include wind direction correction (Wilczak, Oncley & Stage 2001), steady wind selection (Foken *et al.* 2004), thermal stratification stability judgement (Stull 1988) and detrending manipulation (Hutchins *et al.* 2012). The detailed procedure can be found in Liu *et al.* (2023). The corresponding fluctuating signal can be obtained by subtracting the 1 h mean value of the signal after rigorous data pre-processing. The particle-free and particle-laden experimental datasets (fluctuating velocity and corresponding fluctuating PM10 concentration) employed herein were recorded by Wang & Zheng (2016) and Liu *et al.* (2023), respectively. The validation and comparison of the selected data under particle-free and particle-laden conditions are shown in Liu, He & Zheng (2021) and Liu *et al.* (2023) by checking the basic statistics. The particle characteristics parameters (e.g. particle density, response time, Froude number and Stokes number) are listed in table 1, and the detailed calculation procedures of turbulent velocity and particle information can be found in Liu *et al.* (2023). Moreover, as the particle size distribution shown in Liu *et al.* (2023) indicates, there are still larger particles ($>10 \, \mu m$) in particle-laden flows. Due to the constraints of the environment and instruments, it is not feasible to measure effectively the temporal variations of larger particles. In this study, the dust ($<10 \, \mu m$) concentration is considered as the main research object to study their structure characteristics. The flow fields with mean dust concentrations <0.1 and >0.1 mg m^{-3} are considered to be particle-free and particle-laden flows, respectively. The variation of dust concentration collected in the corresponding particle-laden flow field is known as the dust concentration field.

As reported previously (Baars *et al.* 2017; Krug *et al.* 2019; Baars & Marusic 2020*a*), the LCS method employed in this study is effective in extracting wall-attached structures. However, there is no doubt that this method does not exclusively decompose wall-attached self-similar structures: not only wall-attached self-similar structures, but also wall-attached non-self-similar structures are contained (Marusic & Monty 2019; Yoon *et al.* 2020). Deshpande *et al.* (2020) and Deshpande, Monty & Marusic (2021) noted this limitation and described methods (two-dimensional cross-spectrum) to differentiate them. However, due to the limitations of the observation environment, it is difficult to obtain a two-dimensional energy spectrum of the signal under current experimental conditions. So in the current study, no strict distinction is made between wall-attached self-similar structures and wall-attached non-self-similar structures (even though the self-similarity is obvious).

Parameters	Estimation	Ranges
Fluid density, ρ_f (kg m^{-3})	—	1.26
Dissipation rate, ε (m^2 s^{-3})	$\varepsilon = \sigma^3/\kappa z$	0.018–0.33
Kolmogorov time scale, τ_η ($\times 10^{-2}$ s)	$\tau_\eta = (\nu/\varepsilon)^{1/2}$	0.67–2.9
Integral time scale, τ_L (s)	$\tau_L = \int_0^{T_0} R_{uu}(\tau)\,\mathrm{d}\tau$	2.95–9.94
Kolmogorov length scale, η ($\times 10^{-4}$ m)	$\eta = (\nu^3/\varepsilon)^{1/4}$	3.5–7.2
Integral length scale, L (m)	$L = \bar{u}\tau_L$	30–140
Friction Reynolds number, Re_τ ($\times 10^6$)	$Re_\tau = U_\tau \delta/\nu$	1.8–5.2
Particle density, ρ_p (kg m^{-3})	—	2650
Scale ratio (η-based), d_p/η	d_p/η	0.1–0.3
Scale ratio (L-based), d_p/L ($\times 10^{-7}$)	d_p/L	5.15–36.8
Particle response time, τ_p ($\times 10^{-2}$ s)	$\tau_p = \rho_p d_p^2/18\rho_f \nu$	3.13–7.57
Froude number, Fr	$Fr = U_\tau/\tau_p g$	0.38–1.92
Stokes number (η-based), St_η	$St_\eta = \tau_p/\tau_\eta$	1.08–11.29
Stokes number (L-based), St_L ($\times 10^{-2}$)	$St_L = \tau_p/\tau_L$	0.32–2.56
Stokes number (inner-based), St^+	$St^+ = \tau_p U_\tau^2/\nu$	134–1620
Mass loading, Φ_m	$\Phi_m = C/(\rho_f P_d)$	$O(10^{-4})$

Table 1. Basic parameters of fluid and particles in the ASL: σ is the root mean square of the streamwise velocity fluctuation, $\kappa = 0.41$ is the Kármán constant, ν is the kinetic viscosity that is estimated based on the pressure and temperature of the site (Tracy, Welch & Porter 1980), U_τ is the friction velocity, which is estimated as $\sqrt{-\overline{uw}}$ at $z = 2.5$ m following Hutchins *et al.* (2012) and Li & McKenna Neuman (2012), δ is the boundary layer thickness collected by Doppler LiDAR (Liu *et al.* 2023), $\bar{u}$ is the local mean velocity, $R_{uu}(\tau)$ and T_0 are the temporal autocorrelation function and the corresponding first zero-crossing point (Emes *et al.* 2019; Li *et al.* 2021), and C and P_d are the mean concentration and percentage of PM10.

3. Characteristics of the wall-attached structures

To investigate the characteristics of the wall-attached structures, the coherence in different scales based on the LCS are explored first. The coherence spectrogram for the particle-free data with the lowest reference point $z_R/\delta = 0.006$ from the QLOA is shown in figure 2(*a*). The coherence spectrograms are reflected by increasing greyscales. It can be noted that there exists a region in the (λ_x, z) space where γ^2 is the isocontour alignment with lines of constant $\lambda_x/\Delta z$ (with Δz the wall-normal separation to the lowest observation point). In addition, consistent with the results obtained from canonical TBL experiments, with the superposition of hierarchical structures in the flow field, the magnitude of the coherence spectrum in large-scale ranges near the wall is most significant; i.e. increasing coherence accumulates in large-scale components near the wall (Baars *et al.* 2017; Duan *et al.* 2020). In the logarithmic layer, the magnitude of γ^2 increases linearly with $\log(\lambda_x)$ for a constant Δz (which is more intuitive in figure 2*d*), which is the nature of a geometrically self-similar structure (Baars *et al.* 2017; Krug *et al.* 2019). The results indicate that the data collected in the QLOA can effectively capture wall-attached structures through the LCS, similar to the results of laboratory experiments and ASL observations from the SLTEST under near-neutral conditions. Notably, in wall turbulence studies, the lower the reference position ($z_R \to 0$), the greater the amount of wall-attached hierarchical organization of eddies that can be captured. However, because of the limitations of field observation conditions, it is difficult to reach the extreme near-wall position as in laboratory experiments. Therefore, with reference to the available field observations, $z/\delta = 0.006$ is taken as the reference height in this study, which is lower than the reference position in Krug *et al.* (2019). The implied geometrical self-similarity is obviously equivalent to the attached eddy framework discussed above if $\Delta z \approx z$, which is approached
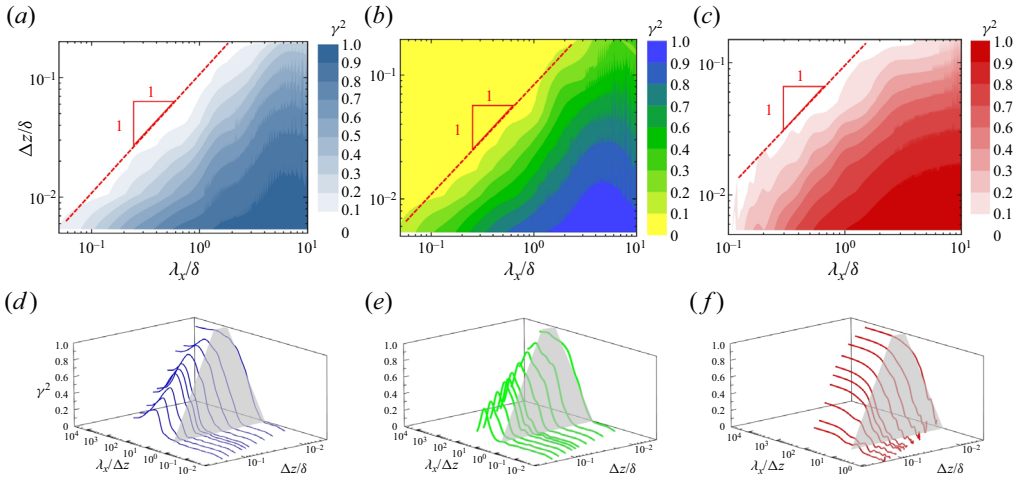
Figure 2. Coherence spectrograms of streamwise velocity fluctuations u in (a) particle-free, (b) particle-laden and (c) dust concentration fluctuations c. (d,e,f) The corresponding three-dimensional coherence spectrograms with the wavelength axis predivided by Δz.

either for $z_R \to 0$ or for $z \gg z_R$ in experiments. For a large Δz, there is no difference between plotting γ^2 as a function of z or Δz, consistent with the expectation at $\Delta z \gg z_R$ (Krug *et al.* 2019). Therefore, in the subsequent study, normalization with Δz is used, as this approach provides a more extensive scaling region. In addition, similar special regions are observed in the particle-laden flow fields (figure 2b) and dust concentration fields (figure 2c) (the variables u in (1.2) are replaced by the dust concentration fluctuations c at the corresponding height). This means that under the influence of particles, wall-attached structures still exist in the particle-laden flow field; moreover, some special particle clustering structures occur in the concentration field.

When the streamwise wavelength is scaled by the local height Δz, the LCS of the dust concentration fluctuation c (figure 2f) obtained synchronously with the streamwise velocity fluctuation u from QLOA shows a signature similar to the LCS of u under particle-free/laden conditions (figures 2d,e) and that in laboratory experiments (Baars *et al.* 2017; Baidya *et al.* 2019). The spectral characteristic of the dust concentration fluctuation c may be analogous to that of the streamwise velocity fluctuation u, i.e. there exists a certain region in (λ_x, Δz) space (shown by the grey inclined plane) where the LCS lines at different heights follow the same increasing pattern with increasing wavelength. The region adheres to

$$\gamma^2 = C_1 \ln(\lambda_x/\Delta z) + C_2, \tag{3.1}$$

where C_1 and C_2 are constants, and the region is consistent with the inclined plane recorded in Baars *et al.* (2017). These signatures are reminiscent of the hierarchy of attached eddies in streamwise velocity fluctuations (Baars *et al.* 2016). This indicates that there are wall-attached dust clustering structures with self-similar nature in the dust concentration field, whose characteristics and differences from those of u need to be clarified further.

After describing the qualitative characteristics of the LCS of u in the flow fields (under particle-free and particle-laden conditions) and those of c in dust concentration fields, the variation in the coherent characteristics with the wall-normal position of the reference point is further investigated. The LCS plots for flow fields under particle-free
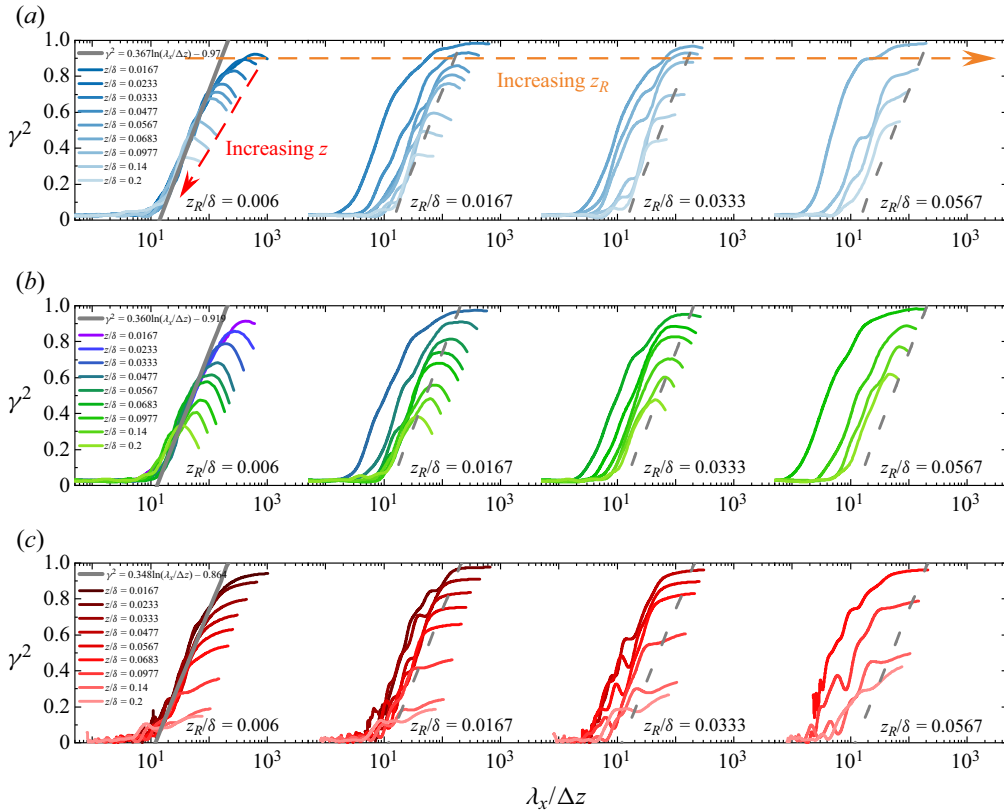
Figure 3. Obtained LCS plots with different reference height z_R: (*a*) results for u in the particle-free flow, (*b*) results for u in particle-laden flow, and (*c*) the corresponding LCS plots for dust concentration fluctuation c. The grey lines are from fitting (3.1). The grey dashed lines are copies of the fitting lines in the leftmost plots.

and particle-laden conditions and for dust concentrations with reference points at $z_R/\delta = 0.006$, 0.0167, 0.0333 and 0.0567 are shown in figures 3(*a*), 3(*b*) and 3(*c*), respectively. As the height of the reference point spans one order of magnitude, the coherence characteristics of both the flow fields and the dust concentration field change significantly. When the reference point is close to the wall ($z_R/\delta = 0.006$), the captured spectra exhibit good collapse, which is consistent with the result from TBLs in Baars *et al.* (2017). This means that the coherent structures captured by the reference point closest to the wall exhibit obvious self-similarity, as described by the classic AEH (the size of the eddy is proportional to its distance from the wall) (Townsend 1976), which can further be used to investigate the scale and energy characteristics of wall-attached structures. In addition, when the traversing points become higher while the reference point is invariant (the red arrow in figure 3), the spectral lines gradually decrease. This is because with increasing height of the traversing point, the captured hierarchies of eddies attached to the wall decrease, and only larger hierarchies can be captured, leading to a lower coherence γ^2.

On the basis of the qualitative variations in the LCS characteristics, the respective LCS plots for different phases (flow field and dust concentration field) in high-Reynolds-number ASLs are further investigated under different conditions. The leftmost plots in figures 3(*a*) and 3(*b*) show the Δz-scaled LCS plots for streamwise velocity fluctuations u in particle-free and particle-laden flows, respectively. The leftmost plot in figure 3(*c*) shows

the Δz-scaled LCS for dust concentration c. Notably, all the LCS plots collapse well within a certain wavelength range, which agrees with the results of existing laboratory particle-free TBL experiments (Baars *et al.* 2017; Baars & Marusic 2020*a*). As discussed in § 2, due to the limitation of the LCS, the wall-attached non-self-similar structures are not completely excluded. However, the present results still exhibit an obvious self-similar nature due to the high-Reynolds-number condition. A high Reynolds number ensures adequate scale separation, which likely results in the inclusion of many structures scaled by z (i.e. self-similar). This means that the energetic wall-attached eddies are predominantly self-similar. Moreover, the spectral characteristic of the dust concentration fluctuation c may be analogous to that of the streamwise velocity fluctuation u. There exists a self-similar region in the spectral space where the LCS lines in the flow and those in the dust concentration field satisfy (3.1). The fitting parameters (C_1, C_2) for streamwise velocity fluctuations under particle-free and particle-laden conditions and for dust concentration are $(0.367 \pm 0.009, -0.97 \pm 0.03)$, $(0.360 \pm 0.002, -0.919 \pm 0.007)$ and $(0.348 \pm 0.003, -0.864 \pm 0.011)$, respectively. Moreover, the minimum streamwise wavelength at which the energetic variance still appears relative to its wall-normal extent is called the aspect ratio (AR) (Baars *et al.* 2017), i.e.

$$AR = \left. \frac{\lambda_x}{z} \right|_{\gamma^2=0} \approx \left. \frac{\lambda_x}{\Delta z} \right|_{\gamma^2=0}$$

$$= \exp\left(-\frac{C_2}{C_1}\right). \tag{3.2}$$

Following the aforementioned approximation, $\lambda_x/\Delta z$ is approximately equal to λ_x/z. The aspect ratios for streamwise velocity fluctuations u under particle-free and particle-laden conditions and for dust concentration c can be obtained based on the definition of the aspect ratio. The results are listed in table 2, and the previously documented laboratory experimental results have also been added for comparison. Based on error propagation (Hughes & Hase 2010), the errors of AR are calculated and added in table 2. The aspect ratio in this study for wall-attached self-similar structures in particle-free flow ($AR_{uf} = 14.1 \pm 1.5$) agrees with the particle-free TBL ($AR = 14$; Baars *et al.* 2017), channel ($AR = 13.9$; Duan *et al.* 2020) and other ASL ($AR = 14$; Krug *et al.* 2019) results, which further validates the reasonability of the reference height used here and the correctness of the results. This reference height can be used to extract wall-attached structures. Based on the same process, the aspect ratios in particle-laden conditions, for wall-attached velocity and concentration structures, are $AR_{ul} = 12.8 \pm 0.3$ and $AR_c = 12.0 \pm 0.5$, respectively. It is worth noting that the aspect ratio for dust concentration is comparable to that for temperature fluctuation ($AR_\theta \approx 10.6$; Krug *et al.* 2019), which is also taken as scalar, and presumably would be equivalent to particles in the low *St* limit. In addition, the results in this study indicate that although the aspect ratios of the wall-attached structures in particle-laden flow and in the dust concentration field are smaller than that in particle-free flow field from the perspective of mean value, this difference is not significant enough under the present conditions when taking provided error ranges into account. However, this decreasing tendency is to be anticipated by the close connection between the aspect ratio and the structure inclination angle. According to the definition of the structure inclination angle (Marusic & Heuer 2007; Liu, Bo & Liang 2017), the larger the structure inclination angle, the smaller the aspect ratio. Tay, Kuhn & Tachie (2015) and Wang, Gu & Zheng (2020) found that the addition of a large number of particles into a particle-laden flow leads to an increase of the inclination angle in the horizontal channel and ASL, respectively. Besides, the variation in the structure inclination

Flow type	Parameter	Aspect ratio
TBL (Baars *et al.* 2016)	u	14
ASL (SLTEST, Krug *et al.* 2019)	u	14
Channel (Duan *et al.* 2020)	u	13.9
ASL (QLOA)	u (particle-free)	14.1 ± 1.5
ASL (QLOA)	u (particle-laden)	12.8 ± 0.3
ASL (QLOA)	c	12.0 ± 0.5

Table 2. Aspect ratios obtained by the LCS for different flow types.

angle can be attributed to the 'stretching' effect of the velocity gradient (Adrian, Meinhart & Tomkins 2000; Dennis 2015), and previous research has suggested that particles lead to a reduction in the velocity gradient and thus increase the structure inclination angle (Wang *et al.* 2020); the aspect ratio is then expected to be reduced.

When the reference point becomes higher (the orange arrow in figure 3), the LCS collapsing characteristics (scaling trends) for both fluctuating velocity (figures 3a,b) and dust fluctuating concentration (figure 3c) are no longer obvious until they disappear ($z_R/\delta = 0.0567$). For further comparison, the fitting lines for $z_R/\delta = 0.006$ are re-plotted to the LCS at each higher reference point, indicated by the grey dashed lines. It can be seen that with the decreasing of the traversing point positions, the corresponding LCS plots become much greater than the expected scaling trends, and the corresponding ratio threshold ($\lambda_x/\Delta z|_{\gamma^2=0}$) decreases. This means that with increasing reference height, the coherent structures captured by the LCS plots not only include the part attached to the wall but also contain large-scale energetic structures that are not attached to the wall (Baars & Marusic 2020a; Hu *et al.* 2020). A similar result also appears in laboratory TBLs, but this phenomenon is not as significant as that in ASLs due to the limitation of the Reynolds number (figure 10 in Baars & Marusic 2020a). This suggests that the non-attached eddies mask the self-similar characteristics of the wall-attached eddies exhibiting the failure of the scaling collapse. As mentioned above, theoretically, the closer the reference position is to the wall, the closer the result is to the AEH. However, limited by the field observation conditions, the lowest observational reference point $z_R/\delta = 0.006$ ($z_R^+ \equiv z_R U_\tau/\nu \sim O(10^4)$) is adopted in this study. This value is much lower than the reference point ($z_R/\delta = 0.0233$) in Krug *et al.* (2019), which also used field data to estimate the flow field coherence through LCS plots. In this situation, $\Delta z \approx z$, the self-similarity for the flow field and that for the dust concentration field are investigated.

4. Spectral scaling of fluctuating streamwise velocity and dust concentration

Self-similar structure characteristics of fluctuating streamwise velocity and dust concentration have been identified, and their aspect ratios have been assessed from the coherence between the turbulence signals at the traversing points and at the near-wall reference point in the flow and dust concentration fields in § 3. On this basis, much attention should be given to the energy, and it is necessary to further investigate the energy spectra of this type of wall-attached structure. To obtain the energy distribution characteristics of these wall-attached eddies in the flow field, spectral linear stochastic estimation (LSE), a data-driven decomposition method, is used to identify attached structures (Adrian 1979; Baars *et al.* 2016; Baars & Marusic 2020a,b). The streamwise velocity fluctuations at the near-wall reference point and at the target point are $u(z_R)$

and $u(z)$, respectively, and the coherent velocity $u_A(z)$ with respect to the reference point (approximately wall-attached) at the target point can be expressed as

$$\hat{u}_A(z; \lambda_x) = H(z, z_R; \lambda_x)\, \hat{u}(z_R; \lambda_x), \tag{4.1}$$

where $H(z, z_R; \lambda_x)$ is the linear transfer kernel computed from

$$
\begin{aligned}
H(z, z_R; \lambda_x) &= \frac{\langle \hat{u}(z; \lambda_x)\, \hat{u}^*(z_R; \lambda_x) \rangle}{\langle \hat{u}(z_R; \lambda_x)\, \hat{u}^*(z_R; \lambda_x) \rangle} \\
&= \frac{\Phi_{uu}(z, z_R; \lambda_x)}{\Phi_{uu}(z_R; \lambda_x)} \\
&= |H(z, z_R; \lambda_x)| \exp(j\varphi(z, z_R; \lambda_x)),
\end{aligned} \tag{4.2}
$$

comprising a wavelength-dependent linear gain $|H|$ and phase φ. Notably, the coherent velocity $\hat{u}_A(z; \lambda_x)$ is not the imprint velocity of the reference velocity for one particular hierarchy eddy, but imprints from other hierarchies of eddies with heights exceeding z (Hu *et al.* 2020). For this reason, the contribution of wall-attached structures to the streamwise turbulence intensity at different heights can be extracted. Furthermore, combining (1.2), (4.1) and (4.2), the coherent energy spectra with the near-wall position at the target point can be expressed as

$$
\begin{aligned}
\Phi_{uu}^A(z; \lambda_x) &= |H(z, z_R; \lambda_x)|^2\, \Phi_{uu}(z_R; \lambda_x) \\
&= \gamma^2\, \Phi_{uu}(z; \lambda_x).
\end{aligned} \tag{4.3}
$$

It can be noticed easily that the kernel for the LSE to detect these structures can be found via the LCS. The energy that is coherent with the wall is part of the total energy. The coherent portion Φ_{uu}^A can be reconstructed via an LSE procedure and is equal to the energy spectra Φ_{uu} at z multiplied by γ^2. As a data-driven scale-dependent filter, γ^2 has the ability to decompose Φ_{uu} or Φ_{cc} into coherent and incoherent portions relative to z_R, following

$$
\begin{aligned}
\underbrace{\Phi_{uu}^N(z; \lambda_x)}_{\text{Wall-incoherent}} &= \underbrace{\Phi_{uu}(z; \lambda_x)}_{\text{Entire energy}} - \underbrace{\gamma^2\, \Phi_{uu}(z; \lambda_x)}_{\text{Wall-coherent}} \\
&= (1 - \gamma^2)\, \Phi_{uu}(z; \lambda_x).
\end{aligned} \tag{4.4}
$$

As derived above, the LCS provides information on how much energy is stochastically coherent/incoherent between z and z_R. In this scenario, take dust concentration ($St_\eta \equiv \tau_p/\tau_f \sim O(10^{-2})$) as an example for illustration. The unfiltered premultiplied spectrum of the dust concentration at $z/\delta = 0.0567$ is shown in figure 4(*a*). The usual reason for premultiplying the spectrum by the wavenumber is to create a logarithmic plot in which equal areas under the curve correspond to equal energies (or variances) (Smits *et al.* 2011). Notably, in the form of a premultiplied energy spectrum, the fluctuation intensity of multi-scale dust concentration lies mainly in $O(10^0) < k_x\delta < O(10^1)$, and the corresponding wavelengths are approximately 0.6δ–6δ. Figure 4(*b*) shows the LCS plots between the target point $z/\delta = 0.0567$ and the near-wall reference point $z/\delta = 0.006$. When outer-scaling is adopted, the LCS reveals that the correlation with the near-wall signal is obvious when the wavenumber is less than 10, while it appears to level off as the wavenumber is less than 1 (Baars *et al.* 2017; Baars & Marusic 2020*a*). On this basis, the LCS is used here as a scale-dependent filter to decompose $\Phi_{cc}(z; \lambda_x)$ into stochastically wall-coherent and wall-incoherent portions, as shown in (4.4); the corresponding results
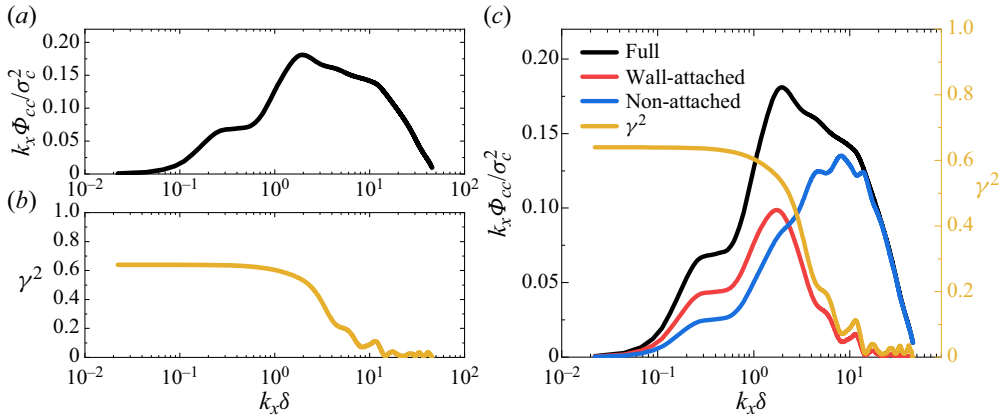
Figure 4. Diagrams of the decomposition of the c spectrum at location $z/\delta = 0.0567$: (*a*) the original energy spectrum, (*b*) the corresponding LCS, and (*c*) the decomposition results for wall-coherent (attached) component (red line) and wall-incoherent (non-attached) component (blue line) of the energy spectrum, via γ^2 filter.

are shown in figure 4(*c*). The black and yellow curves are the unfiltered premultiplied spectrum of the dust concentration and the corresponding LCS, respectively. The red and blue curves are the filtered wall-attached and non-attached portions, respectively. The energy peak from the premultiplied spectra of c contains energies from both wall-attached and non-attached structures. Furthermore, non-attached dust clustering structures are located mainly in the small-scale range, while wall-attached clusters are the dominant structures in the large-scale range. This is anticipated because the smallest coherent motion that can be obtained from the coherence spectrum between two positions amounts to the separation distance; the length scale of the wall-attached structure is larger and the wall-attached structure can be detected more easily, while the smaller scales (the physical height is less than the separation distance) show no coherence.

After performing the aforementioned data-driven decomposition (4.4) for all the energy spectra of the streamwise velocity fluctuations u (in particle-free and particle-laden flows), throughout the entire observation range, the wall-attached and non-attached portions of the energy spectra can be obtained. The energy spectra of the fluctuating streamwise velocity under particle-free and particle-laden conditions with wall-scaling and outer-scaling are plotted in figures 5(*a–c*) and 5(*d–f*), respectively. The unfiltered outer-scaled energy spectra of u are shown in figures 5(*a,d*), and wall-attached spectra with an wall-scaling are shown in figures 5(*b,e*) –and with an outer-scaling in figures 5(*c,f*). Figures 5(*a*) and 5(*d*) show that, regardless of whether the flow is particle-free or particle-laden, the unfiltered energy spectra exhibit a distinct peak that corresponds to the VLSMs in high-Reynolds-number wall-bounded flows, and an obvious pivoting phenomenon, i.e. the premultiplied spectra $k_x \Phi_{uu}/U_\tau^2$ decrease with increasing height in the high-wavenumber region, but increase with height in the low-wavenumber region. This was explained by the 'top-down' mechanism proposed by Hunt & Morrison (2000), where VLSMs are originated in the high position rather than near the wall, carry energy to move downwards, and break into more small-scale eddies near the wall. In other words, whether in particle-free or in particle-laden flows, the energy of this kind of non-attached large-scale structure is superimposed on the energy that can be described by the AEH, which will mask the outer-scaling or wall-scaling characteristics (Hwang *et al.* 2020). For this reason, an increasing number of scholars have proposed many different methodologies
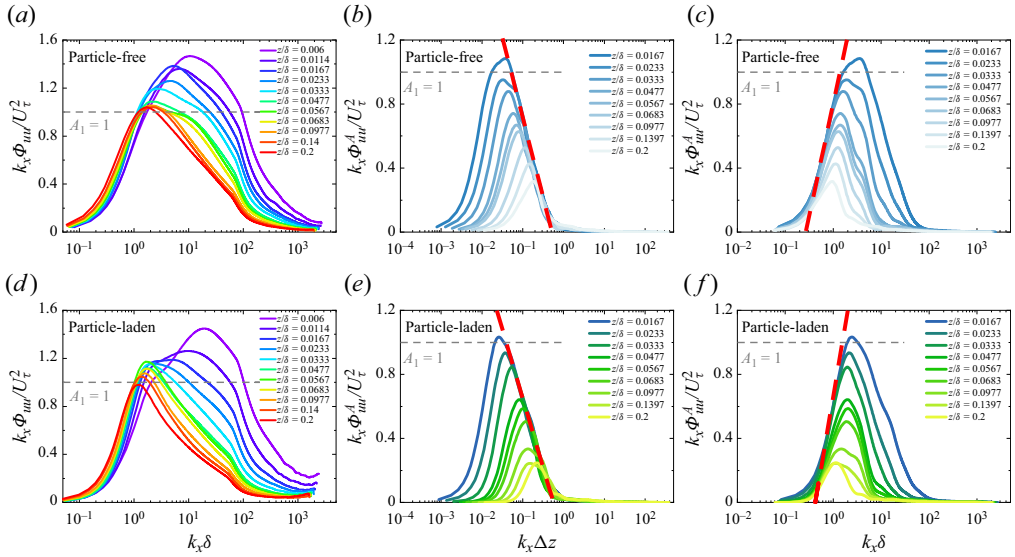
Figure 5. The energy spectra of the streamwise velocity fluctuations *u*: (*a,d*) the original outer-scaling energy spectra, (*b* and *e*) the wall-attached energy spectra scaled by Δz, and (*c,f*) the wall-attached energy spectra scaled by δ. The results under particle-free conditions are shown in the (*a–c*), and the results under particle-laden conditions are shown in (*d–f*).

to decompose or extract the wall-attached components of flow fields (del Álamo *et al.* 2006; Cheng *et al.* 2019; Baars & Marusic 2020*a,b*; Hu *et al.* 2020). However, after extracting the energy of the wall-attached portions by LCS, the decomposed energy spectra show a reasonably good collapse in the medium-wavenumber ranges when scaled with the local heights, and in low-wavenumber ranges when outer-scaled, respectively, i.e. the spectra obey wall-scaling (red dashed lines in figures 5*b,e*) and outer-scaling (red dashed lines in figures 5*c,f*). In addition, the peak magnitudes decay rapidly with increasing *z* position, which is similar to the tendency observed in the TBL (Baars & Marusic 2020*a*). This corresponds to the fact that the number of wall-attached structures in the flow fields decreases gradually with increasing height, and their contributions to energy decrease gradually. Overall, the LCS method where the near-wall signal is employed as the reference signal is effective at extracting the energy components of wall-attached structures that can be described effectively by the AEM from the energy spectra (although the wall-attached non-self-similar structures in ASL are not isolated successfully).

The same data-driven filtering method is used to decompose the premultiplied dust spectra Φ_{cc}, and the decomposed wall-attached portions with wall-scaling (figure 6*b*) and outer-scaling (figure 6*c*) can be obtained from the unfiltered premultiplied dust spectra (figure 6*a*). Figure 6(*a*) shows that the scaling behaviour is not obvious in the unfiltered dust concentration spectra. Moreover, the dust spectra decrease gradually with increasing height at both high and low wavenumbers (i.e. no pivoting phenomenon can be observed), which is different from the trend that the energy fraction of VLSMs increases with wall-normal distance under particle-free and particle-laden conditions in Wang & Zheng (2016) and Liu & Zheng (2021), respectively. Dust emission results mainly from saltation through sandblasting (Dupont 2020). It is when saltating-sand-sized aggregates hit the ground at the downwind end of their trajectories that a fraction of their kinetic energy can be used to eject finer dust particles either from the aggregates themselves or from the soil
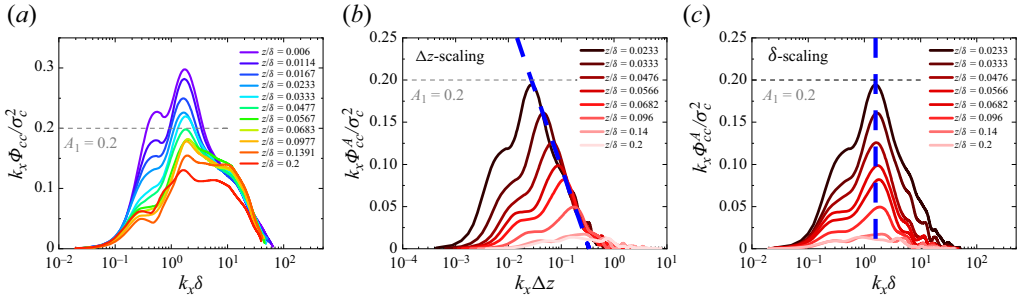
Figure 6. The spectra of the dust concentration fluctuations c: (a) the original spectra of c, (b) the decomposed c spectra scaled by Δz, and(c) the decomposed c spectra scaled by δ.

surface on which they impact (sandblasting process) (Sow *et al.* 2009). Dust particles, once airborne, can be transported by turbulent motions into the upper levels of the atmosphere (Shao 2008). This formation mechanism is quite similar to that of VLSMs in the TBL; hairpin eddies align coherently in packets, and packets line up so that the low momentum flow in the lower part of each packet fits together with the flows in the other packets to form a much longer structure at higher positions (Kim & Adrian 1999). It is reasonable to infer that the formation mechanism of the dust concentration structure is not the result of the coexistence of 'top-down' and 'bottom-up' mechanisms reflected by the formation mechanism of the velocity structure (Wang & Zheng 2016), but rather a single 'bottom-up' mechanism.

In figure 6(b), the spectra of the wall-attached c exhibit reasonable wall-scaling collapse (blue dashed line), which is consistent with the characteristics of the energetic wall-attached eddies described by the AEM, i.e. the energy spectra show good wall-scaling collapse in medium wavenumbers (Perry & Chong 1982). When scaled by the boundary layer thickness δ (as shown in figure 6c), it can be found that VLSMs are still present in the concentration field, but there is a lack of outer-scaling features as in the decomposed velocity fields. In the low-wavenumber (large-scale) ranges, logically speaking, dust has small inertia and a low St, and the dust concentration should follow the attached u behaviour, i.e. meet the outer-scaling (shown in figures 5c,f). However, as the wall-normal distance increases, the intensity of the dust clustering structures satisfying the wall-attached characteristics gradually decreases, and the spectral peak locations are approximately $\lambda_x \approx 5\delta$ in the whole measured region (blue dashed line). This is different from the decomposed spectral characteristics of the wall-attached u structures in TBLs (Baars & Marusic 2020a) and ASLs (shown in figure 5). The absence of the outer-scaling shown in figure 6(c) may means that the wall-attached dust clustering structures cannot maintain the attached VLSMs like those in u components. This may be because the variation of the dust concentration is also affected by the wall-normal velocity fluctuations; the ejection–sweep events (Wallace 2016), which are significant in contributing to the vertical transport of the dust, play a dominant role in the logarithmic layer (Zhang, Hu & Zheng 2018). Moreover, the coherence between the events and the vertical transport of the dust is found to be more significant in larger scales (Li & Bou-Zeid 2011). These large-scale events would ruin the long transport path controlled by the large-scale wall-attached u structures along the streamwise direction. The wall-attached characteristics of dust concentration in large-scale ranges are disrupted, and thus cannot be captured.
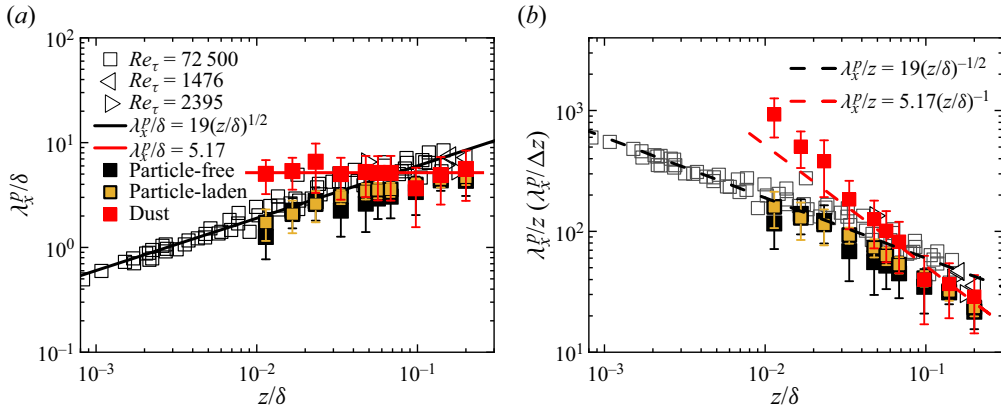
Figure 7. Wavelength of the spectral peak in (*a*) outer-scaling and (*b*) z (or Δz) scaling against z/δ. The black, yellow and red filled symbols are the results of u from particle-free and particle-laden conditions and c, respectively. The error bars represent the corresponding standard deviation. The open symbols are the TBL results from Balakumar & Adrian (2007) ($Re_\tau = 1476, 2395$) and Vallikivi *et al.* (2015*a*) ($Re_\tau = 72\,500$) for wavelengths associated with the lower wavenumber peak (VLSMs, open black symbols).

Notably, a clearly discerned k_x^{-1} spectral region still cannot be observed even under high-Reynolds-number conditions (Morrison *et al.* 2002, 2004; Puccioni *et al.* 2023). Chandran *et al.* (2017) predicted that an appreciable k_x^{-1} scaling region can appear only for $Re_\tau > 60\,000$ (from examination of two-dimensional, streamwise–spanwise u spectra). Note that the aforementioned analysis holds for $z^+ = 150$ and that a k_x^{-1} region is expected to shrink linearly with z, meaning that $Re_\tau \sim O(10^6)$ is required for $\Phi_{uu} \propto k_x^{-1}$ at $z^+ = 1000$ (Baars & Marusic 2020*a*). Unfortunately, limited by the field observation conditions, the lowest observation point is $x/\delta \approx 0.006$ ($z^+ \equiv zU_\tau/\nu \sim O(10^4)$), which is quite a bit higher than the position where an obvious k_x^{-1} region can be found. To further investigate the spectral scaling of the fluctuating streamwise velocity and dust concentration, following Chandran *et al.* (2017) and Deshpande *et al.* (2020), the peak (or 'ridge') wavelength of the decomposed spectra of the streamwise velocity fluctuation (black and yellow filled symbols, respectively) and the dust concentration (red symbols) are summarized in figure 7. Besides, the TBL results from Balakumar & Adrian (2007) ($Re_\tau = 1476, 2395$) and Vallikivi, Ganapathisubramani & Smits (2015*a*) ($Re_\tau = 72\,500$) for wavelengths associated with the lower wavenumber peak (VLSMs, open black symbols) are added for comparison. Figure 7(*a*) shows that the wavelengths of the streamwise velocity fluctuations in particle-free and particle-laden conditions are in good agreement with the TBL results (Balakumar & Adrian 2007; Vallikivi *et al.* 2015*a*), satisfying the 1/2 power scaling law of the local height z and the ASL thickness δ, i.e. $\lambda_x^p/\delta = 19(z/\delta)^{1/2}$. However, for the decomposed dust concentration fluctuation c, even after decomposition, it does not display a trend consistent with the flow field results, exhibiting the independence on the wall-normal location, i.e. $\lambda_x^p/\delta = 5.17$. This means that the scales of most-energetic wall-coherent dust clusters are almost invariant within the observation range. Correspondingly, for the z (or Δz) scaling in figure 7(*b*), the results of turbulent velocity and dust concentration follow the relations $\lambda_x^p/z = 19(z/\delta)^{-1/2}$ and $\lambda_x^p/z = 5.17(z/\delta)^{-1}$, respectively. The streamwise scale of dust is much larger than that of streamwise velocity; the scales of the two gradually converge as the height increases.
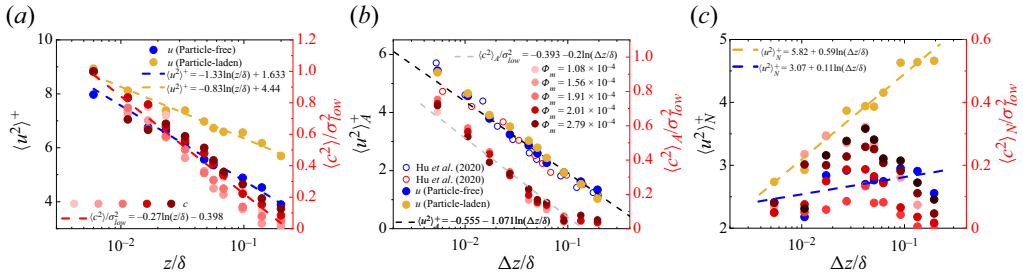
986 A21-16

Figure 8. (*a*) Streamwise turbulence intensity $\langle u^2 \rangle^+$ and dust concentration variance $\langle c^2 \rangle / \sigma_{low}^2$ versus wall-normal location. (*b*) Wall-attached part of the turbulence intensity $\langle u^2 \rangle_A^+$ and dust concentration variance $\langle c^2 \rangle_A / \sigma_{low}^2$ with wall-normal location. (*c*) The non-attached parts $\langle u^2 \rangle_N^+$ and $\langle c^2 \rangle_N / \sigma_{low}^2$ vary with wall-normal location.

5. Discussion on Townsend–Perry constant A_1

After providing the spectral scaling characteristics with different length scales in streamwise velocity fluctuations and dust concentration fluctuations in particle-free and particle-laden flows, the streamwise turbulence intensity (dust concentration variance) against the wall-normal distance can be obtained by integrating the corresponding spectra in Fourier space. The integrated results are shown in figure 8(*a*). The blue filled and yellow filled symbols are the streamwise turbulence intensities in the particle-free and particle-laden conditions, respectively. The red filled symbols are the dust concentration intensities with different particle mass loadings. The variation in the streamwise turbulence intensity exhibits wall-normal logarithmic decay throughout the logarithmic region, and the streamwise turbulence intensity is enhanced in particle-laden flows, which is consistent with the tendency in the ASL results (Liu *et al.* 2023). Moreover, the dust concentration variance also follows a nearly logarithmic decay in the wall-normal direction. However, the turbulence (and dust) intensity logarithmic decay slopes exhibit significant differences in the particle-free and particle-laden flows.

The variations in the decomposed wall-attached streamwise turbulence intensity $\langle u^2 \rangle_A^+$ are shown in figure 8(*b*), where the red and blue open symbols are the ASL streamwise turbulence intensities associated with the attached eddies extracted by a scale-based filter from Hu *et al.* (2020). It can be noted that streamwise turbulence intensities show no significant difference in particle-free and particle-laden flows, and they still meet the logarithmic-linear manner described by the AEH and are consistent with the slopes recorded in Hu *et al.* (2020) ($A_1 = 1$ for TBL and ASL) and Baars & Marusic (2020*b*) ($A_1 = 0.98$ for TBL). This indicates that the Townsend–Perry constant A_1 seems invariant with respect to the particle concentration. In addition, except for the logarithmic slope, the magnitude of the turbulence intensity in particle-laden flow shows no obvious difference from that in particle-free flow, and is consistent with the attached-eddy-type turbulence intensity extracted by the different method from Hu *et al.* (2020) within a similar Re_τ range, which means that particles do not destroy the statistical characteristics of attached eddies.

In addition to the streamwise turbulence intensity in u, the wall-attached dust concentration intensity ($\langle c^2 \rangle_A$) shows similar logarithmic decay after scale-dependent decomposition by the filter γ^2. The corresponding slope is approximately 0.2, which is smaller than that for the flow field ($A_1 = 1$) and the decay slope for the unfiltered dust concentration (0.27). In addition, the wall-attached dust concentration intensity is close to 0 at the top of the logarithmic layer, which could be attributed to the spatial coherence that

is responsible for the wall-attached dust clustering structures breaking down in the outer region of the flow (Marusic 2001), resulting in the absence of wall-attached dust clustering structures in the outer region. It should be emphasized that the results for different mass loadings seem invariant, and always remain at 0.2, i.e. the decay slope has no particle mass loading effect. This means that the attached eddy structures in wall turbulence have a certain capacity for transporting dust particles, and show no dependence on the particle mass loading. Here, the variance of the dust concentration at the lowest measurement point is employed for normalization, which is similar to the treatment used in Talluru, Philip & Chauhan (2018) for normalizing the concentration of tracer gas. This process has an impact on the magnitude of the decomposed dust concentration intensity, but has no impact on the overall trend.

On the other hand, the corresponding non-attached intensity ($\langle u^2 \rangle_N^+$ and $\langle c^2 \rangle_N$) can be obtained by subtracting the original turbulence (dust) intensity, as shown in figure 8(*c*). There are significant differences between the wall-attached and non-attached portions. The non-attached energy in particle-free flows (blue filled symbols) slightly increases with wall-normal distance (shown by the blue dashed line), while that in particle-laden flows is significantly enhanced by the addition of particles (shown by the yellow dashed line). Combined with the total turbulence intensity (figure 8*a*) and the wall-attached energy (figure 8*b*) in particle-free and particle-laden flows, it can be considered that the decrease of slope (A_1) in particle-laden flow can be attributed to the influence of particles on the non-attached eddy structures. Moreover, the variation in dust intensity for non-attached portions is different from that for flows, i.e. the peak value of the intensity is located at approximately the midpoint of the logarithmic layer, and the intensity gradually decreases both sides of the midpoint. To some extent, this means that the characteristics of the non-attached dust clustering structures in the dust concentration field are similar to those of wall-detached eddies in the flow field (Hu *et al.* 2020), i.e. the wall-detached energy increases with wall-normal distance as far as at the midpoint of the logarithmic layer, and then decreases as wall-normal distance continues to increase. In addition, with the increase of particle mass loading, the dust intensity of the non-attached portion gradually increases, showing an obvious mass loading dependence, while this dependence is not obvious in the wall-attached portion shown in figure 8(*b*). This suggests that the influence of particles is reflected mainly in the non-attached structures rather than in the wall-attached structures.

In the study of canonical wall turbulence, the streamwise turbulence intensity follows a logarithmic decay with wall-normal distance *z*, and the decay slope A_1 (the Townsend–Perry constant) has received much attention over the past decades with the development of experiments and the improvement of numerical simulations. The decay slope A_1 for wall-attached portions can be obtained by fitting the data with (1.1). Figure 9 shows the logarithmic decay slopes under particle-free (black filled square) and particle-laden (yellow filled circle) conditions. Since the energies of the wall-attached structures have been extracted by the LCS described in § 4, the slopes of the corresponding wall-attached portions are added in figure 9 (shown by blue filled squares and circles, respectively).

In addition, the previous results for high-Reynolds-number wall turbulence are also presented in figure 9 for comparison. The black open squares are the results from TBLs for $68\,780 < Re_\tau < 628\,000$ and from ASLs ($Re_\tau \sim O(10^6)$) (Marusic *et al.* 2013), the black upward-pointing triangles are from the TBL experiment ($Re_\tau < 19300$) (Baars & Marusic 2020*b*), the black downward-pointing triangles are the direct numerical simulations results from channel flow with $Re_\tau = 8000$ by Yamamoto & Tsuji (2018), the black diamond points are from Laval *et al.* (2017), and the black open circles are the results from fully
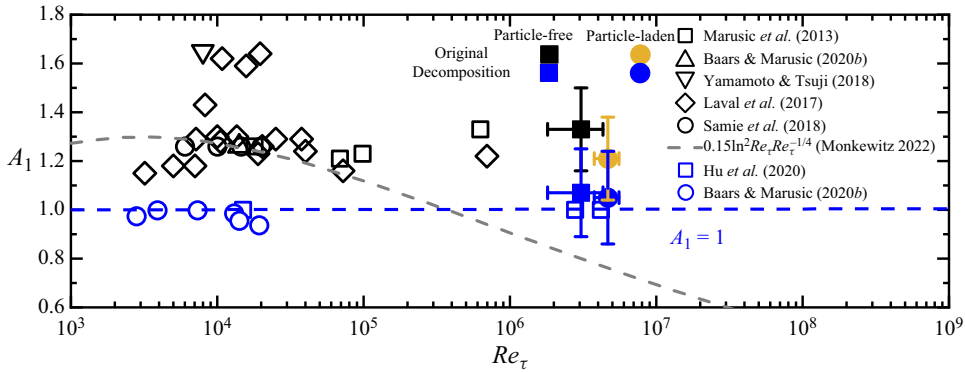
Figure 9. Townsend–Perry constant versus Re_τ. Black filled square and yellow filled circle symbols are the turbulent velocity fluctuations in particle-free and particle-laden conditions, respectively. Blue filled square and circle symbols are the decomposed results in particle-free and particle-laden conditions, respectively. The error bars in the abscissa and ordinate axes represent the corresponding standard deviations of Reynolds number and Townsend–Perry constants for all the selected near-neutral ASL datasets, respectively. The open symbols are the particle-free results from Marusic *et al.* (2013), Laval *et al.* (2017), Samie *et al.* (2018), Yamamoto & Tsuji (2018), Baars & Marusic (2020b) and Hu *et al.* (2020). The grey dashed line is the asymptotic formulation of the logarithmic slope derived in Monkewitz (2022).

resolved measurements of TBLs for the Reynolds number range $Re_\tau = 6000$–$20\,000$ from Samie *et al.* (2018). In addition to the experimental and numerical results, the asymptotic formulation of the slope for $\langle u^2 \rangle^+$ (shown by the grey dashed line) proposed by Monkewitz (2022) is also added; when $Re_\tau \to \infty$, this slope asymptotically approaches $A_1 = 0$. The decay slopes of the energy from the wall-attached eddies obtained by different decomposition methods are additionally plotted for comparison. The blue open circles are the results from Baars & Marusic (2020b) obtained by data-driven LCS decomposition, and the blue open squares are the slopes from Hu *et al.* (2020) obtained by spectral decomposition for extracting part of the velocity field.

The decay slopes, i.e. the Townsend–Perry constants, show significant differences between the original and decomposed results. First, focusing on the original logarithmic slope, although the logarithmic scaling of the streamwise velocity variance is found, the slopes of the scaling law are not entirely consistent. The slope of A_1 is close to 1.26 (Marusic *et al.* 2013; Samie *et al.* 2018) for many moderate-Reynolds-number flows, but there are still some results that show relatively small or large values. These variations in A_1 are due largely to the varying streamwise turbulence intensity decay slope with Re_τ (Baars & Marusic 2020b; Hu *et al.* 2020; Hwang *et al.* 2022; Monkewitz 2022). With the increase in the Reynolds number, an increasing number of non-attached eddies with significant Reynolds dependence will become obvious far from the wall (Hu *et al.* 2020). In this scenario, the slope of non-decomposed $\langle u^2 \rangle^+$ includes the energy decay of non-attached type energy superimposed on top of the attached eddy decay (Baars & Marusic 2020b). As the Reynolds number tends to infinity, the logarithmic slope may tend to 0 according to the asymptotic formula given by Monkewitz (2022). However, the AEM envisions a constant A_1 in (1.1), which is invariant with Re_τ. The core of this mismatch is a simple fact, i.e. in actual measures of the total streamwise turbulence intensity, other non-attached contributions are present (Baars & Marusic 2020b; Hu *et al.* 2020). This means that this type of energetic non-attached eddy structure seems to mask the pure AEM behaviour in flows. Similarly, after adding the particles, the slope of the streamwise turbulence intensity decreases as the intensity of the non-attached eddy with particle dependence is more

significantly enhanced far from the wall (yellow filled symbols in figure 9 and the results in Liu *et al.* 2023).

For this reason, many researchers have focused on extracting/decomposing eddies or flow fields to obtain the A_1 described by the AEM. Notably, even though the techniques for extracting wall-attached structures in the flow field are different in existing studies, the corresponding obtained Townsend–Perry constants are similar (as shown by the blue symbols in figure 9). Baars & Marusic (2020b) provided some evidence for a Townsend–Perry constant $A_1 = 0.98$, which would describe the wall-normal logarithmic decay of the turbulence intensity per Townsend's AEH. Hu *et al.* (2020) extracted the part of the flow associated with the attached eddy, and found that $A_1 = 1$ for TBL and ASL. In this study, similar results are given from the statistical characteristics of the flow field excluding the non-attached eddies by the LCS. In particle-free flows, $A_1 = 1.07$ is consistent with the existing decomposed Townsend–Perry constant. In addition, different from the variation in the decay slope in the original streamwise turbulence intensity, the decomposed turbulence intensity in particle-laden flows is invariant, which means that the AEM is further verified and that the particles do not destroy the statistical characteristics of the attached eddies in particle-laden flows.

On the other hand, considering that the Townsend–Perry constant is associated with the one-dimensional energy spectrum (as noted in Chandran *et al.* 2017; Baars & Marusic 2020a; Deshpande *et al.* 2021), going back to figure 5, the Townsend–Perry constant A_1, the theoretical plateau value of the attached eddy energy spectrum, is added for comparison. It can be seen easily that in the full-scale energy spectra (figures 5a,d), the energy for other types of the eddy (e.g. non-attached eddies) superposed on that of the attached eddy would mislead the Townsend–Perry constant A_1 belonging to the AEH. After the decomposition by LCS, the magnitudes of the decomposed spectra (in Δz-scaling (figures 5b,e) and outer-scaling (figures 5c,f)) peaks are quite close to the Townsend–Perry constant. The amplitudes of the peaks decay rapidly with increasing z. This is consistent with the observations of Baars & Marusic (2020a), following the prediction of the AEH that a smaller population of wall-attached eddies exists keeping away from the wall (Townsend 1976). Combined with the previous results and existing studies, it can be claimed that the near-wall high mass loading particles act as aerodynamic roughness and influence the fluid flow scale outside the sand saltation layer (Zheng, Feng & Wang 2021; Liu *et al.* 2023), but the formation mechanics of the eddies are still applicable (Townsend 1976).

Finally, the same process is applied to the dust concentration, and the variation in the intensity of the dust concentration with wall-normal distance is discussed. The trends for dust concentration are similar to the results for the flow field, but there are obvious differences in the decay slopes between the decomposed dust concentration ($A_1 = 0.2$) and the decomposed flow field ($A_1 = 1$). It is anticipated from figure 8 that as the normalization parameters are different for velocity and dust concentration (friction velocity and variance of the dust concentration, respectively), the decay slopes are quite different from each other. Besides, similar to the results from figures 5(a) and 5(d), the variation of the dust concentration induced by the other types of eddies may disguise the actual A_1 attributed to wall-attached dust concentration (figure 6a). The magnitudes of decomposed dust concentration spectra peaks (figures 6b,c) are quite close to the decay slope ($A_1 = 0.2$). With a gradual increase in height, similar to the characteristics of the decomposed velocity energy spectra, the peaks gradually decrease. This means that the variation of the dust concentration induced by the attached eddy is decreasing with increasing height. It can be conjectured reasonably that, similarly to the flow field results,

the expected plateau region occurs and becomes more visible when the height is lower (Chandran *et al.* 2017; Baars & Marusic 2020*a*).

6. Concluding remarks

The wall-attached structure characteristics of streamwise velocity fluctuations u under particle-free/laden conditions and dust concentration fluctuations c are investigated in this study based on high-Reynolds-number ($Re_\tau \sim O(10^6)$) synchronous multiphase observations from the QLOA site (recorded by Liu *et al.* 2023). The results show that not only the particle-free flow field, but also the particle-laden flow and dust concentration field contain wall-attached structures with self-similar natures, which is similar to the experimental results and is consistent with the classic AEH in the wall turbulence community. The aspect ratios captured in particle-free flow, particle-laden flow and dust concentration field are approximately 14.1, 12.8 and 12.0, respectively.

The abundant non-attached turbulent structures in the flow field and the induced dust clustering structures in the concentration field mask the scaling behaviour in the energy spectra. After using the data-driven spectral filters on streamwise velocity fluctuations u and on the dust concentration fluctuations c, the original premultiplied energy spectra can be decomposed into wall-attached and non-attached portions. For the undecomposed spectra, unlike the pivoting phenomenon observed in u (the premultiplied spectra decrease with increasing height in the high-wavenumber region, but increase with height in the low-wavenumber region), the c spectra decrease gradually with increasing height at both high and low wavenumbers. The decomposed wall-attached u energy spectra exhibit wall-scaling and outer-scaling behaviour in the medium-wavenumber and low-wavenumber ranges, respectively, which is consistent with the AEM. Interestingly, the decomposed wall-attached spectra of c obey wall-scaling in the medium-wavenumber range, while outer-scaling is absent in the low-wavenumber range. The streamwise length of the most significant wall-attached dust clustering structures in the logarithmic region is approximately five times the boundary layer thickness, and does not change significantly with height.

The streamwise turbulence intensity is significantly enhanced with the addition of particles, and the corresponding logarithmic decay slope (Townsend–Perry constant) A_1 is reduced. However, the affected portions are non-attached structures, and the wall-attached portions are invariant after adding particles, which still meets $A_1 = 1$, as reported in laboratory experiments and numerical simulations. Particles do not destroy the statistical characteristics of wall-attached structures. Moreover, the wall-attached portion of the dust (particle size smaller than $10\,\mu\text{m}$) concentration also exhibits a universal logarithmic decay slope and without the particle mass loading effect (under the condition $\Phi_m \sim O(10^{-4})$), while the remaining non-attached portions have a significant particle mass loading dependence.

Declaration of interests. The authors report no conflict of interest.

Author ORCIDs.

Ⓓ Xibo He https://orcid.org/0000-0003-0788-3566;

Ⓓ Hongyou Liu https://orcid.org/0000-0002-2444-543X;

Ⓓ Xiaojing Zheng https://orcid.org/0000-0002-6845-2949.

REFERENCES

ADRIAN, R.J. 1979 Conditional eddies in isotropic turbulence. *Phys. Fluids* **22** (11), 2065–2070.

ADRIAN, R.J., MEINHART, C.D. & TOMKINS, C.D. 2000 Vortex organization in the outer region of the turbulent boundary layer. *J. Fluid Mech.* **422**, 1–54.

DEL ÁLAMO, J.C., JIMÉNEZ, J., ZANDONADE, P. & MOSER, R.D. 2006 Self-similar vortex clusters in the turbulent logarithmic region. *J. Fluid Mech.* **561**, 329.

BAARS, W.J., HUTCHINS, N. & MARUSIC, I. 2016 Spectral stochastic estimation of high-Reynolds-number wall-bounded turbulence for a refined inner–outer interaction model. *Phys. Rev. Fluids* **1** (5), 054406.

BAARS, W.J., HUTCHINS, N. & MARUSIC, I. 2017 Self-similarity of wall-attached turbulence in boundary layers. *J. Fluid Mech.* **823**, R2.

BAARS, W.J. & MARUSIC, I. 2020*a* Data-driven decomposition of the streamwise turbulence kinetic energy in boundary layers. Part 1. Energy spectra. *J. Fluid Mech.* **882**, A25.

BAARS, W.J. & MARUSIC, I. 2020*b* Data-driven decomposition of the streamwise turbulence kinetic energy in boundary layers. Part 2. Integrated energy. *J. Fluid Mech.* **882**, A26.

BAIDYA, R., *et al.* 2019 Simultaneous skin friction and velocity measurements in high Reynolds number pipe and boundary layer flows. *J. Fluid Mech.* **871**, 377–400.

BAKER, L., FRANKEL, A., MANI, A. & COLETTI, F. 2017 Coherent clusters of inertial particles in homogeneous turbulence. *J. Fluid Mech.* **833**, 364–398.

BALACHANDAR, S. & EATON, J.K. 2010 Turbulent dispersed multiphase flow. *Annu. Rev. Fluid Mech.* **42** (1), 111–133.

BALAKUMAR, B.J. & ADRIAN, R.J. 2007 Large- and very-large-scale motions in channel and boundary-layer flows. *Phil. Trans. R. Soc. Lond.* A **365**, 665–681.

BERK, T. & COLETTI, F. 2020 Transport of inertial particles in high-Reynolds-number turbulent boundary layers. *J. Fluid Mech.* **903**, A18.

BERNARDINI, M., PIROZZOLI, S. & ORLANDI, P. 2013 The effect of large-scale turbulent structures on particle dispersion in wall-bounded flows. *Intl J. Multiphase Flow* **51**, 55–64.

BRANDT, L. & COLETTI, F. 2022 Particle-laden turbulence: progress and perspectives. *Annu. Rev. Fluid Mech.* **54** (1), 159–189.

CHANDRAN, D., BAIDYA, R., MONTY, J.P. & MARUSIC, I. 2017 Two-dimensional energy spectra in high-Reynolds-number turbulent boundary layers. *J. Fluid Mech.* **826**, R1.

CHENG, C., LI, W., LOZANO-DURÁN, A. & LIU, H. 2019 Identity of attached eddies in turbulent channel flows with bidimensional empirical mode decomposition. *J. Fluid Mech.* **870**, 1037–1071.

CUI, G., RUHMAN, I. & JACOBI, I. 2022 Spatial detection and hierarchy analysis of large-scale particle clusters in wall-bounded turbulence. *J. Fluid Mech.* **942**, A52.

DENNIS, D.J.C. 2015 Coherent structures in wall-bounded turbulence. *An. Acad. Bras. Ciênc.* **87** (2), 1161–1193.

DESHPANDE, R., CHANDRAN, D., MONTY, J.P. & MARUSIC, I. 2020 Two-dimensional cross-spectrum of the streamwise velocity in turbulent boundary layers. *J. Fluid Mech.* **890**, R2.

DESHPANDE, R., MONTY, J.P. & MARUSIC, I. 2021 Active and inactive components of the streamwise velocity in wall-bounded turbulence. *J. Fluid Mech.* **914**, A5.

DUAN, Y., ZHANG, P., ZHONG, Q., ZHU, D. & LI, D. 2020 Characteristics of wall-attached motions in open channel flows. *Phys. Fluids* **32** (5), 055110.

DUPONT, S. 2020 Scaling of dust flux with friction velocity: time resolution effects. *J. Geophys. Res.* **125** (1), e2019JD031192.

ELGHOBASHI, S. & TRUESDELL, G.C. 1992 Direct simulation of particle dispersion in a decaying isotropic turbulence. *J. Fluid Mech.* **242**, 655–700.

EMES, M.J., ARJOMANDI, M., KELSO, R.M. & GHANADI, F. 2019 Turbulence length scales in a low-roughness near-neutral atmospheric surface layer. *J. Turbul.* **20** (9), 545–562.

FOKEN, T., GOCKEDE, M., MAUDER, M., MAHRT, L., AMIRO, B. & MUNGER, W. 2004 Post-field data quality control. In *Handbook of Micrometeorology: A Guide for Surface Flux Measurement and Analysis* (ed. X. Lee, W. Massman & B. Law), pp. 181–208. Kluwer Academic.

GUALA, M., HOMMEMA, S.E. & ADRIAN, R.J. 2006 Large-scale and very-large-scale motions in turbulent pipe flow. *J. Fluid Mech.* **554**, 521.

HE, X. & LIU, H. 2023 The effect of turbulent motions on particle spatial distribution in high-Reynolds-number particle-laden flows. *J. Fluid Mech.* **976**, A14.

HELLSTRÖM, L.H.O., MARUSIC, I. & SMITS, A.J. 2016 Self-similarity of the large-scale motions in turbulent pipe flow. *J. Fluid Mech.* **792**, R1.

HÖGSTRÖM, U., HUNT, J.C.R. & SMEDMAN, A.S. 2002 Theory and measurements for turbulence spectra and variances in the atmospheric neutral surface layer. *Boundary-Layer Meteorol.* **103** (1), 101–124.

Hu, R., Yang, X.I.A. & Zheng, X. 2020 Wall-attached and wall-detached eddies in wall-bounded turbulent flows. *J. Fluid Mech.* **885**, A30.

Hughes, I. & Hase, T. 2010 *Measurements and their Uncertainties: A Practical Guide to Modern Error Analysis*. Oxford University Press.

Hunt, J.C.R. & Morrison, J.F. 2000 Eddy structure in turbulent boundary layers. *Eur. J. Mech.* B **19** (5), 673–694.

Hutchins, N., Chauhan, K., Marusic, I., Monty, J. & Klewicki, J. 2012 Towards reconciling the large-scale structure of turbulent boundary layers in the atmosphere and laboratory. *Boundary-Layer Meteorol.* **145** (2), 273–306.

Hwang, J., Lee, J.H. & Sung, H.J. 2020 Statistical behaviour of self-similar structures in canonical wall turbulence. *J. Fluid Mech.* **905**, A6.

Hwang, J. & Sung, H.J. 2018 Wall-attached structures of velocity fluctuations in a turbulent boundary layer. *J. Fluid Mech.* **856**, 958–983.

Hwang, J. & Sung, H.J. 2019 Wall-attached clusters for the logarithmic velocity law in turbulent pipe flow. *Phys. Fluids* **31** (5), 055109.

Hwang, Y., Hutchins, N. & Marusic, I. 2022 The logarithmic variance of streamwise velocity and k^{-1} conundrum in wall turbulence. *J. Fluid Mech.* **933**, A8.

Jie, Y., Cui, Z., Xu, C. & Zhao, L. 2022 On the existence and formation of multi-scale particle streaks in turbulent channel flows. *J. Fluid Mech.* **935**, A18.

Jiménez, J. 2012 Cascades in wall-bounded turbulence. *Annu. Rev. Fluid Mech.* **44** (1), 27–45.

Jiménez, J. & Hoyas, S. 2008 Turbulent fluctuations above the buffer layer of wall-bounded flows. *J. Fluid Mech.* **611**, 215–236.

Kaftori, D., Hetsroni, G. & Banerjee, S. 1995a Particle behavior in the turbulent boundary layer. 1. Motion, deposition, and entrainment. *Phys. Fluids* **7** (5), 1095–1106.

Kaftori, D., Hetsroni, G. & Banerjee, S. 1995b Particle behavior in the turbulent boundary layer. 2. Velocity and distribution profiles. *Phys. Fluids* **7** (5), 1107–1121.

Kiger, K.T. & Pan, C. 2002 Suspension and turbulence modification effects of solid particulates on a horizontal turbulent channel flow. *J. Turbul.* **3**, N19.

Kim, K.C. & Adrian, R.J. 1999 Very large-scale motion in the outer layer. *Phys. Fluids* **11** (2), 417–422.

Krug, D., Baars, W.J., Hutchins, N. & Marusic, I. 2019 Vertical coherence of turbulence in the atmospheric surface layer: connecting the hypotheses of Townsend and Davenport. *Boundary-Layer Meteorol.* **172** (2), 199–214.

Laval, J.P., Vassilicos, J.C., Foucaut, J.M. & Stanislas, M. 2017 Comparison of turbulence profiles in high-Reynolds-number turbulent boundary layers and validation of a predictive model. *J. Fluid Mech.* **814**, R2.

Li, B. & McKenna Neuman, C. 2012 Boundary-layer turbulence characteristics during aeolian saltation. *Geophys. Res. Lett.* **39** (11), L11402.

Li, C., Lim, K., Berk, T., Abraham, A., Heisel, M., Guala, M., Coletti, F. & Hong, J. 2021 Settling and clustering of snow particles in atmospheric turbulence. *J. Fluid Mech.* **912**, A49.

Li, D. & Bou-Zeid, E. 2011 Coherent structures and the dissimilarity of turbulent transport of momentum and scalars in the unstable atmospheric surface layer. *Boundary-Layer Meteorol.* **140** (2), 243–262.

Liu, H., Bo, T. & Liang, Y. 2017 The variation of large-scale structure inclination angles in high Reynolds number atmospheric surface layers. *Phys. Fluids* **29** (3), 035104.

Liu, H., He, X. & Zheng, X. 2021 An investigation of particles effects on wall-normal velocity fluctuations in sand-laden atmospheric surface layer flows. *Phys. Fluids* **33** (10), 103309.

Liu, H., He, X. & Zheng, X. 2023 Amplitude modulation in particle-laden atmospheric surface layers. *J. Fluid Mech.* **957**, A14.

Liu, H. & Zheng, X. 2021 Large-scale structures of wall-bounded turbulence in single- and two-phase flows: advancing understanding of the atmospheric surface layer during sandstorms. *Flow* **1**, E5.

Lozano-Durán, A., Flores, O. & Jiménez, J. 2012 The three-dimensional structure of momentum transfer in turbulent channels. *J. Fluid Mech.* **694**, 100–130.

Marchioli, C. & Soldati, A. 2002 Mechanisms for particle transfer and segregation in a turbulent boundary layer. *J. Fluid Mech.* **468**, 283–315.

Marusic, I. 2001 On the role of large-scale structures in wall turbulence. *Phys. Fluids* **13** (3), 735–743.

Marusic, I., Baars, W.J. & Hutchins, N. 2017 Scaling of the streamwise turbulence intensity in the context of inner–outer interactions in wall turbulence. *Phys. Rev. Fluids* **2** (10), 100502.

Marusic, I. & Heuer, W.D.C. 2007 Reynolds number invariance of the structure inclination angle in wall turbulence. *Phys. Rev. Lett.* **99** (11), 114504.

MARUSIC, I., MCKEON, B.J., MONKEWITZ, P.A., NAGIB, H.M., SMITS, A.J. & SREENIVASAN, K.R. 2010 Wall-bounded turbulent flows at high Reynolds numbers: recent advances and key issues. *Phys. Fluids* **22** (6), 065103.

MARUSIC, I. & MONTY, J.P. 2019 Attached eddy model of wall turbulence. *Annu. Rev. Fluid Mech.* **51** (1), 49–74.

MARUSIC, I., MONTY, J.P., HULTMARK, M. & SMITS, A.J. 2013 On the logarithmic region in wall turbulence. *J. Fluid Mech.* **716**, R3.

MARUSIC, I. & PERRY, A.E. 1995 A wall-wake model for the turbulence structure of boundary layers. Part 2. Further experimental support. *J. Fluid Mech.* **298**, 389–407.

MAXEY, M.R. 1987 The gravitational settling of aerosol particles in homogeneous turbulence and random flow fields. *J. Fluid Mech.* **174**, 441–465.

MCLAUGHLIN, J.B. 1989 Aerosol particle deposition in numerically simulated channel flow. *Phys. Fluids* **1** (7), 1211–1224.

MONKEWITZ, P.A. 2022 Asymptotics of streamwise Reynolds stress in wall turbulence. *J. Fluid Mech.* **931**, A18.

MORRISON, J.F., JIANG, W., MCKEON, B.J. & SMITS, A.J. 2002 Reynolds number dependence of streamwise velocity spectra in turbulent pipe flow. *Phys. Rev. Lett.* **88** (21), 214501.

MORRISON, J.F., MCKEON, B.J., JIANG, W. & SMITS, A.J. 2004 Scaling of the streamwise velocity component in turbulent pipe flow. *J. Fluid Mech.* **508**, 99–131.

NIÑO, Y. & GARCIA, M.H. 1996 Experiments on particle–turbulence interactions in the near-wall region of an open channel flow: implications for sediment transport. *J. Fluid Mech.* **326**, 285–319.

ÖRLÜ, R., FIORINI, T., SEGALINI, A., BELLANI, G., TALAMELLI, A. & ALFREDSSON, P.H. 2017 Reynolds stress scaling in pipe flow turbulence – first results from CICLoPE. *Phil. Trans. R. Soc.* A **375** (2089), 20160187.

PERRY, A.E. & ABELL, C.J. 1977 Asymptotic similarity of turbulence structures in smooth- and rough-walled pipes. *J. Fluid Mech.* **79** (4), 785–799.

PERRY, A.E. & CHONG, M.S. 1982 On the mechanism of wall turbulence. *J. Fluid Mech.* **119**, 173–217.

PERRY, A.E., HENBEST, S. & CHONG, M.S. 1986 A theoretical and experimental study of wall turbulence. *J. Fluid Mech.* **165**, 163–199.

PICANO, F., SARDINA, G. & CASCIOLA, C.M. 2009 Spatial development of particle-laden turbulent pipe flow. *Phys. Fluids* **21** (9), 093305.

PUCCIONI, M., CALAF, M., PARDYJAK, E.R., HOCH, S., MORRISON, T.J., PERELET, A. & IUNGO, G.V. 2023 Identification of the energy contributions associated with wall-attached eddies and very-large-scale motions in the near-neutral atmospheric surface layer through wind LiDAR measurements. *J. Fluid Mech.* **955**, A39.

ROBINSON, S.K. 1991 Coherent motions in the turbulent boundary layer. *Annu. Rev. Fluid Mech.* **23**, 601–639.

SAMIE, M., MARUSIC, I., HUTCHINS, N., FU, M.K., FAN, Y., HULTMARK, M. & SMITS, A.J. 2018 Fully resolved measurements of turbulent boundary layer flows up to $Re_\tau = 20\,000$. *J. Fluid Mech.* **851**, 391–415.

SARDINA, G., PICANO, F., SCHLATTER, P., BRANDT, L. & CASCIOLA, C.M. 2011 Large scale accumulation patterns of inertial particles in wall-bounded turbulent flow. *Flow Turbul. Combust.* **86** (3–4), 519–532.

SARDINA, G., SCHLATTER, P., BRANDT, L., PICANO, F. & CASCIOLA, C.M. 2012 Wall accumulation and spatial localization in particle-laden wall flows. *J. Fluid Mech.* **699**, 50–78.

SHAO, Y.P. 2008 *Physics and Modelling of Wind Erosion*, 2nd edn. Springer.

SHAUGHNESSY, E.J. & MORTON, J.B. 1977 Laser light-scattering measurements of particle concentration in a turbulent jet. *J. Fluid Mech.* **80**, 129–148.

SMITS, A.J., MCKEON, B.J. & MARUSIC, I. 2011 High-Reynolds number wall turbulence. *Annu. Rev. Fluid Mech.* **43** (1), 353–375.

SOW, M., ALFARO, S.C., RAJOT, J.L. & MARTICORENA, B. 2009 Size resolved dust emission fluxes measured in Niger during 3 dust storms of the AMMA experiment. *Atmos. Chem. Phys.* **9** (12), 3881–3891.

SQUIRES, K.D. & EATON, J.K. 1991 Preferential concentration of particles by turbulence. *Phys. Fluids* **3** (5), 1169–1178.

STULL, R.B. 1988 *An Introduction to Boundary Layer Meteorology*. Springer.

TALLURU, K.M., PHILIP, J. & CHAUHAN, K.A. 2018 Local transport of passive scalar released from a point source in a turbulent boundary layer. *J. Fluid Mech.* **846**, 292–317.

TAY, G.F.K., KUHN, D.C.S. & TACHIE, M.F. 2015 Effects of sedimenting particles on the turbulence structure in a horizontal channel flow. *Phys. Fluids* **27** (2), 025106.

TOWNSEND, A.A. 1976 *The Structure of Turbulent Shear Flow*, 2nd edn. Cambridge University Press.

TRACY, C.R., WELCH, W.R. & PORTER, W.P. 1980 *Properties of Air: A Manual for Use in Biophysical Ecology*, 3rd edn. The University of Wisconsin.

VALLIKIVI, M., GANAPATHISUBRAMANI, B. & SMITS, A.J. 2015*a* Spectral scaling in boundary layers and pipes at very high Reynolds numbers. *J. Fluid Mech.* **771**, 303–326.

VALLIKIVI, M., HULTMARK, M. & SMITS, A.J. 2015*b* Turbulent boundary layer statistics at very high Reynolds number. *J. Fluid Mech.* **779**, 371–389.

WALLACE, J.M. 2016 Quadrant analysis in turbulence research: history and evolution. *Annu. Rev. Fluid Mech.* **48** (1), 131–158.

WANG, G., GU, H. & ZHENG, X. 2020 Large scale structures of turbulent flows in the atmospheric surface layer with and without sand. *Phys. Fluids* **32** (10), 106604.

WANG, G. & RICHTER, D. 2020 Multiscale interaction of inertial particles with turbulent motions in open channel flow. *Phys. Rev. Fluids* **5** (4), 044307.

WANG, G. & ZHENG, X. 2016 Very large scale motions in the atmospheric surface layer: a field investigation. *J. Fluid Mech.* **802**, 464–489.

WILCZAK, J.M., ONCLEY, S.P. & STAGE, S.A. 2001 Sonic anemometer tilt correction algorithms. *Boundary-Layer Meteorol.* **99** (1), 127–150.

WYNGAARD, J.C. 1992 Atmospheric turbulence. *Annu. Rev. Fluid Mech.* **24** (1), 205–234.

YAMAMOTO, Y. & TSUJI, Y. 2018 Numerical evidence of logarithmic regions in channel flow at $Re_\tau = 8000$. *Phys. Rev. Fluids* **3** (1), 012602.

YOON, M., HWANG, J., YANG, J. & SUNG, H.J. 2020 Wall-attached structures of streamwise velocity fluctuations in an adverse-pressure-gradient turbulent boundary layer. *J. Fluid Mech.* **885**, A12.

ZHANG, Y., HU, R. & ZHENG, X. 2018 Large-scale coherent structures of suspended dust concentration in the neutral atmospheric surface layer: a large-eddy simulation study. *Phys. Fluids* **30** (4), 046601.

ZHENG, X., FENG, S. & WANG, P. 2021 Modulation of turbulence by saltating particles on erodible bed surface. *J. Fluid Mech.* **918**, A16.

ZHOU, A. & KLEWICKI, J. 2015 Properties of the streamwise velocity fluctuations in the inertial layer of turbulent boundary layers and their connection to self-similar mean dynamics. *Intl J. Heat Fluid Flow* **51**, 372–382.